Coherent Two-Dimensional Terahertz Magnetic Resonance Spectroscopy of Collective Spin Waves

Jian Lu, Xian Li, Harold Y. Hwang, Benjamin K. Ofori-Okai, Takayuki Kurihara, Tohru Suemoto, and Keith A. Nelson

Coherent Two-Dimensional Terahertz Magnetic Resonance Spectroscopy of Collective Spin Waves

Jian Lu,[1] Xian Li,[1] Harold Y. Hwang,[1] Benjamin K. Ofori-Okai,[1]

Takayuki Kurihara,[2] Tohru Suemoto,[2] and Keith A. Nelson[1, *]

[1]*Department of Chemistry, Massachusetts Institute of Technology, Cambridge, MA 02139, USA*
[2]*Institute for Solid State Physics, The University of Tokyo, Kashiwa, Chiba 277-8581, Japan*
(Dated: April 19, 2017)

We report a demonstration of two-dimensional terahertz (2D THz) magnetic resonance spectroscopy using the magnetic fields of two time-delayed THz pulses. We apply the methodology to directly reveal the nonlinear responses of collective spin waves (magnons) in a canted antiferromagnetic crystal. The 2D THz spectra show all of the third-order nonlinear magnon signals including magnon spin echoes, and 2-quantum signals that reveal pairwise correlations between magnons at the Brillouin zone center. We also observe second-order nonlinear magnon signals showing resonance-enhanced second-harmonic and difference-frequency generation. Numerical simulations of the spin dynamics reproduce all of the spectral features in excellent agreement with the experimental 2D THz spectra.

Nonlinear manipulation of spins is the basis for all advanced methods in magnetic resonance including multidimensional nuclear magnetic resonance and electron spin resonance (ESR) spectroscopies [1, 2], magnetic resonance imaging, and, in recent years, quantum control over individual spins [3]. The methodology is facilitated by the ease with which the regime of strong coupling can be reached between radiofrequency or microwave magnetic fields and nuclear or electron spins respectively, typified by sequences of magnetic pulses that control the magnetic moment directions [1–3]. The capabilities meet a bottleneck, however, for far-infrared magnetic resonances characteristic of correlated electron materials, molecular magnets, and metalloproteins.

ESR in the terahertz (THz) frequency region can reveal rich information content in chemistry, biology, and materials science [1, 2, 4–7]. In molecular complexes and metalloproteins, THz-frequency zero-field splittings (ZFS) of high-spin transition-metal and rare-earth ions show exquisite sensitivity to ligand geometries, providing mechanistic insight into molecular magnetic properties [4] and protein catalytic function [5]. With strong applied magnetic fields ($\sim$10 T), resonances of unpaired electron spins in molecular complexes can be shifted from the usual microwave regime into the THz range, drastically improving the resolution due to enhanced spectral splittings [2, 6, 7]. In many ferromagnetic (FM) and antiferromagnetic (AFM) materials, intrinsic magnetic fields in the same range put collective spin waves (magnons) in the THz range. Current ESR spectroscopy remains limited at THz frequencies because the weak sources used only permit measurements of free-induction decay (FID) signals that are linearly proportional to the excitation magnetic field strength. In some cases, including most proteins, even linear THz-frequency ESR signals may not be measurable because the THz spectrum includes much stronger absorption features due to low-frequency motions of polar segments [8]. However, the fast dephasing of such motions ensures that they would not compete with nonlinear spin echo signals [9]. Two-dimensional (2D) THz ESR spectroscopy, like 2D ESR at lower frequencies, could provide extensive insight into spin interactions and dynamics in these systems. The extension of established, commercially available methodologies in multidimensional magnetic resonance spectroscopy to the THz frequency range will find a wide range of applications spanning multiple disciplines.

Magnons in materials with spin order such as FM and AFM phases have been studied with continuous-wave and pulsed THz fields, revealing the magnon frequencies through their FID signals [10, 11] and demonstrating linear superposition in the responses to time-delayed pulse pairs [11, 12]. Nonlinear spectroscopy and coherent control could unravel complex spin interactions in AFM-to-FM order switching [13], colossal magnetoresistance [14], and multiferroicity [15], and could enable new applications in quantum computing [16], nonvolatile memory [17] and spintronics [18] at unprecedented time scales [19–21]. THz nonlinear spectroscopy and coherent control have been demonstrated recently in various systems, almost exclusively utilizing THz electric fields [22]. So far there are very limited examples of nonlinear THz resonant driving of spins [23] and none in which distinct nonlinear responses are separated from linear responses and from each other as is typical in 2D magnetic resonance spectroscopy.

Here we explore the nonlinearity of magnons using time-delayed intense THz pulse pairs. We develop 2D THz magnetic resonance spectroscopy which can be understood in terms of multiple field-spin interactions that generate the nonlinear signal fields, similar to conventional 2D magnetic resonance but in the low-order perturbative regime more typical of 2D optical spectroscopies. Magnons are resonantly excited without promoting electrons to excited states (as in most spintronics excitation) and hence the observed nonlinearities are of
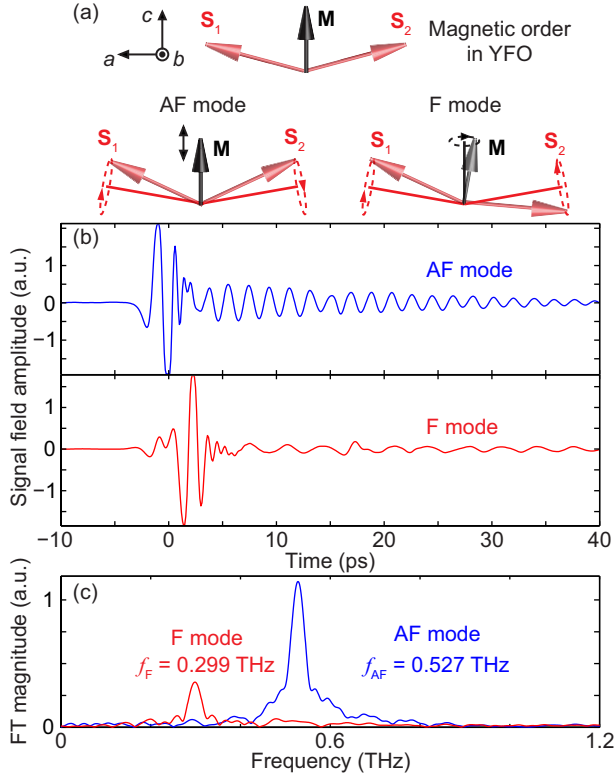
FIG. 1. (a) The canted AFM order in YFO leads to a net magnetization $\mathbf{M}$ along the crystal c-axis. $\mathbf{S}_1$ and $\mathbf{S}_2$ are the Fe^{3+} electron spins ordered along the crystal a-axis. The AF mode is the amplitude oscillation of $\mathbf{M}$ while the F mode the precession of $\mathbf{M}$. (b) Single THz pulses transmitted through the sample followed by FID signals from the AF (blue) and F (red) modes. (c) FT magnitude spectra of the FID signals from both magnon modes, showing magnon resonances at $f_{AF} = 0.527$ THz and $f_F = 0.299$ THz.

purely magnetic origin.

The material under study is a single-crystal (a-cut, 2-mm thickness) YFeO$_3$ (YFO). The ground state has canted AFM order [10, 24] with a net magnetization $\mathbf{M}$ along crystal c-axis as shown in Fig. 1(a) [11, 25, 26] (for details see Fig. S1 in [27]). Two THz-active magnon modes, the quasi-AFM (AF) and quasi-FM (F) modes, can be constructed based on different cooperative motions of sublattice spins $\mathbf{S}_1$ and $\mathbf{S}_2$. Macroscopically the AF mode corresponds to amplitude oscillation of $\mathbf{M}$ and the F mode to precession of $\mathbf{M}$. In YFO at room temperature, the AF mode at $f_{AF} = 0.527$ THz and the F mode at $f_F = 0.299$ THz can be selectively excited by orienting the crystal such that $\mathbf{M}$ is parallel and perpendicular respectively to the THz magnetic field polarization. Upon THz excitation, magnons radiate FID signals $B(t)$ at their frequencies, revealing the linear-response spin dynamics. We measured the FID signal fields for each magnon mode shown in Fig. 1(b) through time-dependent electro-optic sampling (EOS) measurement [28] of the associated electric field. Fourier trans-
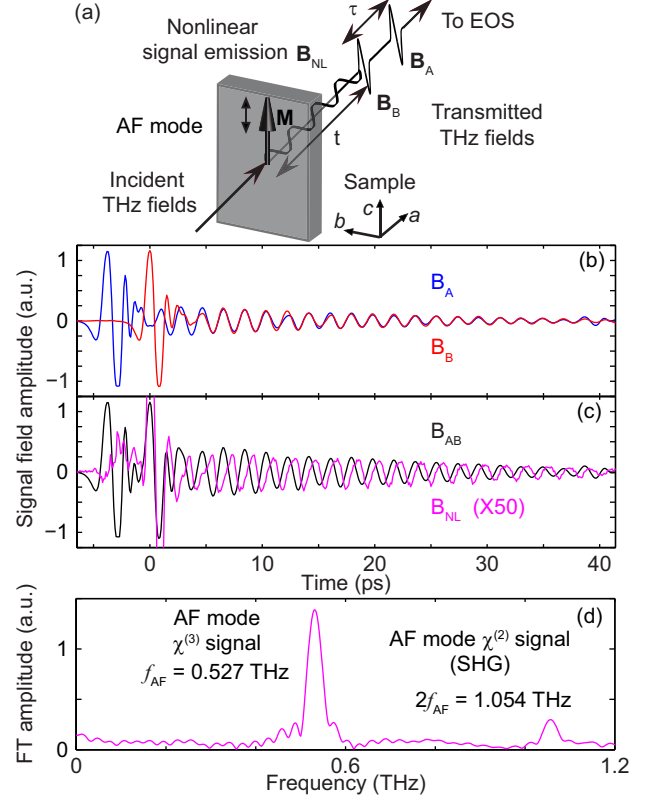

FIG. 2. (a) Schematic experimental geometry. Two THz pulses delayed by τ with magnetic field polarization parallel to $\mathbf{M}$ excite the AF mode. At each delay τ, $\mathbf{B}_{NL}(\tau, t)$ copolarized with input THz magnetic fields is measured by EOS as a function of t. Rotating the sample about the crystal a-axis by $90°$ such that $\mathbf{M}$ is perpendicular to the THz magnetic fields allows the measurement of the F mode. (b) AF mode magnon signals induced by THz pulse A ($\mathbf{B}_A$, blue) and B ($\mathbf{B}_B$, red) individually. (c) Magnon signal with the presence of both THz pulses at $\tau = 3.7$ ps ($\mathbf{B}_{AB}$, black) and nonlinear signal ($\mathbf{B}_{NL}$ magnified 50x, magenta). (d) FT magnitude spectrum of the oscillatory signal in $\mathbf{B}_{NL}$ reveals $\chi^{(3)}$ and $\chi^{(2)}$ peaks at f_{AF} and $2f_{AF}$.

formation (FT) of the FID yields the linear spectrum for each magnon mode shown Fig. 1(c).

Figure 2(a) shows the experimental geometry schematically (for details see Section 2 in [27]). Two collinearly propagating single-cycle THz pulses denoted as A and B were generated in a LiNbO$_3$ crystal by optical rectification utilizing the tilted-pulse-front technique [29, 30]. THz pulses A and B both with magnetic field polarization (horizontal in the laboratory frame) parallel to $\mathbf{M}$ were focused onto the sample, resulting in magnetic field strengths $B_A = 0.14$ T and $B_B = 0.11$ T (corresponding to $E_A = 420$ kV/cm and $E_B = 340$ kV/cm), to excite the AF mode. Rotating the sample about the crystal a-axis by 90 degrees such that $\mathbf{M}$ was perpendicular to the
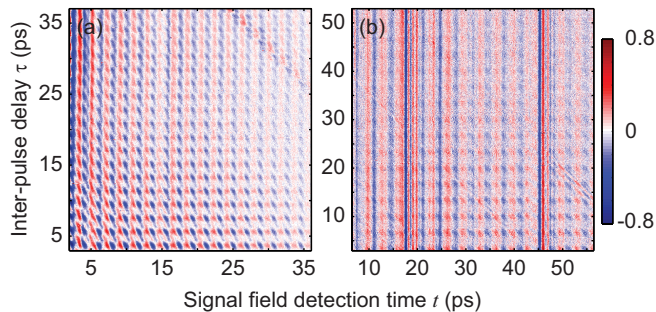
FIG. 3. Normalized 2D time-time plots of $\mathbf{B}_{\mathrm{NL}}(t,\tau)$ from the AF (a) and F (b) mode magnons respectively. Amplitudes exceeding ± 0.8 are saturated in the colormap.

THz magnetic field polarization allowed excitation of the F mode. In each geometry, at an inter-pulse delay τ we recorded the coherent time-dependent signal field $\mathbf{B}(t,\tau)$ emerging from the sample by EOS. We implemented a differential chopping detection method [31] to isolate the nonlinear signal resulting from magnons interacting with both THz pulses. The nonlinear signal field $\mathbf{B}_{\mathrm{NL}}$ is

$$\mathbf{B}_{\mathrm{NL}}(t,\tau) = \mathbf{B}_{AB}(t,\tau) - \mathbf{B}_{A}(t,\tau) - \mathbf{B}_{B}(t), \quad (1)$$

where $\mathbf{B}_{AB}$ is the signal with both THz pulses present, and $\mathbf{B}_A$ and $\mathbf{B}_B$ are signals with THz pulse A and B present individually. As an example, we show in Figs. 2 (b) and 2(c) the t-dependent signals $\mathbf{B}_A$, $\mathbf{B}_B$, $\mathbf{B}_{AB}$ and $\mathbf{B}_{\mathrm{NL}}$ from the AF mode at a delay $\tau = 3.7$ ps (twice the AF mode period). The amplitude in $\mathbf{B}_{AB}$ is coherently enhanced as the magnon coherences induced by each THz pulse are in phase [11, 12]. In $\mathbf{B}_{\mathrm{NL}}$, a phase shift of $3\pi/2$ with respect to $\mathbf{B}_{AB}$ and asymmetric distortion are noticeable. The shifted phase is that of the $\chi^{(3)}$ magnon response. The asymmetry indicates a $\chi^{(2)}$ signal from second harmonic generation (SHG). Both features are resolved in the FT spectrum of the oscillatory signal in $\mathbf{B}_{\mathrm{NL}}$, revealing the $\chi^{(3)}$ and $\chi^{(2)}$ spectral peaks at f_{AF} and $2f_{\mathrm{AF}}$ respectively as shown in Fig. 2(d).

The experimental 2D time-domain traces $\mathbf{B}_{\mathrm{NL}}(t,\tau)$ for each magnon mode in YFO are displayed in Fig. 3. Oscillations along the τ axis reveal the dependence of the nonlinear signal on particular frequency components of the incident THz fields, and oscillations along the t axis reveal the frequency components in the nonlinear signal field. 2D FT of time-domain traces $\mathbf{B}_{\mathrm{NL}}(t,\tau)$ with respect to τ and t yields 2D spectra as functions of excitation frequency ν and detection frequency f. The 2D magnitude spectrum for each magnon mode is shown in Figs. 4(a) and 4(c). The difference in phase accumulation of the induced magnon coherence during time periods τ and t allows the 2D spectra to be separated into nonrephasing (NR) and rephasing (R) quadrants with correspondingly positive and negative values of ν. Along $\nu = 0$ there is a pump-probe (PP) spectral peak which
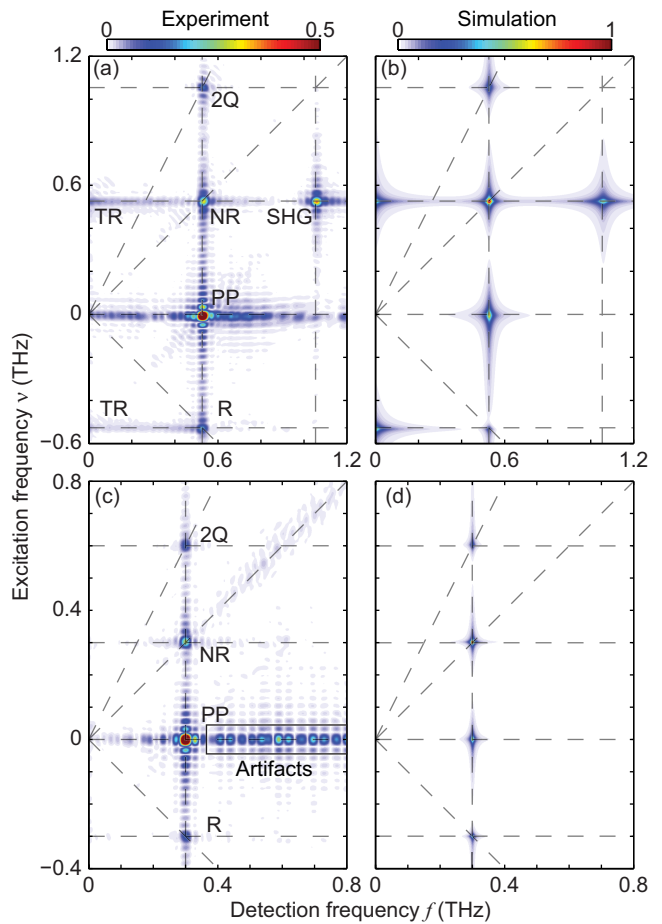

FIG. 4. 2D THz magnetic resonance spectra of magnons in YFO. (a),(b) Experimental (a) and simulated (b) AF mode 2D magnitude spectra. $\chi^{(3)}$ spectral peaks include rephasing (R), nonrephasing (NR), pump-probe (PP) and 2-quantum (2Q) peaks. $\chi^{(2)}$ peaks include second harmonic generation (SHG) and THz rectification (TR) peaks. (c),(d) Experimental (c) and simulated (d) F mode 2D magnitude spectra showing the full set of $\chi^{(3)}$ peaks. The artifacts are due to the signal double-reflections in the sample. Each spectrum is normalized to its maximum amplitude. Amplitudes above 0.5 in (a) and (c) are saturated in the colormap.

results from THz-field-induced magnon population without phase accumulation.

The 2D spectrum for each magnon mode shows the complete set of $\chi^{(3)}$ nonlinear signals which are observed experimentally for the first time in THz-frequency spin systems. The R (spin echo [9]) and NR peaks each result from a single field interaction during pulse A that creates a first-order magnon 1-quantum coherence (1QC). After delay τ, two field interactions during pulse B generate a magnon population and then a third-order 1QC, which is either phase-reversed (R) or not (NR) relative to the first-order 1QC, radiating the nonlinear signal. The 2Q peak arises from two field interactions during pulse A that create a second-order magnon 2-quantum coher-

ence (2QC) accumulating phase at twice the magnon frequency and, after time τ, one field interaction during pulse B that induces transitions to a third-order 1QC radiating the signal. The 2Q signal reveals correlations between pairs of zone-center magnons [32] which are distinct from zone-boundary magnon correlations revealed in 2-magnon Raman spectra [33]. The PP signal is generated by two field interactions during pulse A that create a magnon population and, after delay τ, one interaction with pulse B that generates a third-order 1QC radiating the signal. The $\chi^{(3)}$ peak at f_{AF} shown above in Fig. 2(d) is a sum of these signals at the selected $\tau = 3.7$ ps. Additional $\chi^{(2)}$ spectral peaks due to SHG and THz rectification (TR) are identified in the AF mode 2D spectrum. The signals are emitted by a $\chi^{(2)}$ magnetization resulting from sum- and difference-frequency mixing of the magnon coherences generated by each THz pulse,

$$\mathbf{M}^{(2)}(2\omega_{AF}) = \chi^{(2)}(2\omega_{AF}; \omega_{AF}, \omega_{AF})\mathbf{B}(\omega_{AF})\mathbf{B}(\omega_{AF}) \quad (2)$$

$$\mathbf{M}^{(2)}(0) = \chi^{(2)}(0; -\omega_{AF}, \omega_{AF})\mathbf{B}^*(\omega_{AF})\mathbf{B}(\omega_{AF}). \quad (3)$$

The assignment of the signal in each pathway is further elaborated in Section 6 of [27]. The orders of the nonlinear signals are confirmed by field dependence measurements (see Section 3 in [27]).

Numerical calculations of the sublattice spin dynamics based on the Landau-Lifshitz-Gilbert (LLG) equation were performed to help understand the microscopic origins of the signals observed. The LLG equation used (Section 4, [27]) is derived from the Hamiltonian [34]

$$H = -J\mathbf{S}_1 \cdot \mathbf{S}_2 + \mathbf{D} \cdot (\mathbf{S}_1 \times \mathbf{S}_2) - \sum_{i=1,2}(K_a S_{ia}^2 + K_c S_{ic}^2)$$
$$- \gamma(\mathbf{B}_A^{THz}(t,\tau) + \mathbf{B}_B^{THz}(t)) \cdot \sum_{i=1,2} \mathbf{S}_i. \quad (4)$$

The first term describes the AFM coupling between neighboring spins $\mathbf{S}_1$ and $\mathbf{S}_2$ with a negative exchange constant J. The second term describes the Dzyaloshinskii-Moria (DM) interaction with the antisymmetric exchange parameter $\mathbf{D}$ a vector along the crystal b-axis. The interplay between them results in the canted AFM order shown in Fig. 1(a). The third term accounts for the orthorhombic crystalline anisotropy along crystal a- and c-axes manifested as the ZFS of the unpaired spins of the high-spin Fe^{3+}. The last term is the Zeeman interaction between spins and THz magnetic fields, with γ the gyromagnetic ratio. Numerically solving the LLG equation with the input THz magnetic pulse pair copolarized along either crystal c- or b-axes, we obtained two vectorial solutions of the net magnetization $\mathbf{M}$. We extracted the nonlinear temporal responses of $|\mathbf{M}|$ and M_b with the THz magnetic fields polarized along the crystal a- and b-axis respectively, corresponding to the experimental observables $\mathbf{B}_{NL}$ for each mode. 2D FT yielded the simulated 2D spectrum of each magnon mode shown in Figs. 4(b) and 4(d), exhibiting excellent agreement with

the experimental results. Note that in the simulations, neither the THz electric fields nor any non-magnetic responses were considered, which confirms the magnetic origin of the observed nonlinearity.

In the simulation of the F mode, $\chi^{(2)}$ signals were observed, which were found to emerge from the time-varying M_c (see Section 5 and Fig. S8 in [27]). Although $\chi^{(2)}$ signal polarizations are perpendicular to the incident THz magnetic fields in the case of F mode (i.e. type-II $\chi^{(2)}$ processes), EOS detection would still allow for the detection of the former [35]. However, the birefringent YFO crystal has a large difference between the THz refractive indices along the crystal b- and c-axes, along which the fundamental and $\chi^{(2)}$ THz magnetic fields are polarized respectively. The crystal thickness used is much larger than the coherence length for the type-II SHG and TR (see Section 5 in [27]). The absence of $\chi^{(2)}$ signals in the F mode experimental data is hence attributed to phase mismatching. In the case of the AF mode, phase mismatching for the type-I $\chi^{(2)}$ signals is determined by crystal dispersion and is expected to be much smaller than that of the F mode. Analyzing the trajectories of $\mathbf{S}_1$ and $\mathbf{S}_2$ we note that the SHG and TR signals are due to large-angle spin precessions [36] (for details see Section 7 in [27]). The maximum excursions of $\mathbf{S}_1$ and $\mathbf{S}_2$ from their orientations at equilibrium are estimated to be $\pm 0.5°$ under our THz magnetic fields. Comparing simulations with and without the DM interaction (i.e. canted AFM order versus perfect AFM order), we found that the $\chi^{(2)}$ responses in each magnon mode were observed only with the DM term. As is discussed in [37], the SHG signals should cancel perfectly in a perfect AFM system even in the large-angle precession regime. In YFO where the DM interaction results in canted AFM order, the nonlinear motions of each sublattice spin along the direction of $\mathbf{M}$ do not cancel perfectly. The SHG signal appears in the large-angle precession regime because the magnetization $\mathbf{M}$ is saturable [37] (for details see Section 7 in [27]). This is consistent with our simulation results showing $\chi^{(2)}$ signals in both magnon modes that are parallel to $\mathbf{M}$. Magnetization-induced SHG has been observed in ferromagnetic systems in the microwave frequency range [36], but rectification signals have not been observed before. The connection between SHG and 2Q signals, which derive from the same 2-magnon coherences, is also newly observed. The 2-magnon coherences can radiate directly at the magnon second-harmonic frequency if phase matching is satisfied or can be projected by a third field interaction to 1QCs that radiate at the magnon frequency. In the latter case, even if phase matching is not fulfilled, 2Q signals are still observable in the 2D spectra. See Section 5 of [27] for further discussion. It is also worth noting that in a perfect AFM system, 2-magnon coherences which are not observable by magnon SHG signal emission or optical detection such as Faraday rotation, are expected to appear

In conclusion, we have demonstrated 2D magnetic resonance spectroscopy of THz-frequency magnons and directly observed nonlinear spin responses. The method is generalizable to other THz-frequency magnetic resonances such as spin transitions in molecular complexes and biomolecules with high ZFS. Further enhancement of the THz magnetic fields by novel THz sources [38], magnetic metamaterials [23], and resonant cavities will reveal magnetic nonlinearities far beyond the present perturbative regime such as anharmonic couplings between magnetic modes and anharmonic magnetic potentials [23] in rare-earth orthoferrites and other magnetic systems, which will be manifested respectively by off-diagonal peaks and anharmonic shifts of the diagonal peaks [39]. The methodology enables study of coupled degrees of freedom in various systems such as multiferroics utilizing both THz magnetic and electric fields. THz magnetic fields approaching π pulse areas may enable coherent control over magnetic domain orientations [40] and promising applications in magnon spintronics [18].

---

[*] kanelson@mit.edu

[1] V. S. Bajaj, M. L. Mak-Jurkauskas, M. Belenky, J. Herzfeld, and R. G. Griffin, Proc. Natl. Acad. Sci. U.S.A. **106**, 9244 (2009).

[2] P. Borbat, A. Costa-Filho, K. Earle, J. Moscicki, and J. Freed, Science **291**, 266 (2001).

[3] F. H. L. Koppens, C. Buizert, K.-J. Tielrooij, I. Vink, K. Nowack, T. Meunier, L. Kouwenhoven, and L. Vandersypen, Nature (London) **442**, 766 (2006).

[4] G. A. Craig and M. Murrie, Chem. Soc. Rev. **44**, 2135 (2015).

[5] G. Hanson and L. Berliner, eds., *High resolution EPR: applications to metalloenzymes and metals in medicine* (Springer, New York, USA, 2009).

[6] K. K. Andersson, P. P. Schmidt, B. Katterle, K. R. Strand, A. E. Palmer, S.-K. Lee, E. I. Solomon, A. Gräslund, and A.-L. Barra, J. Biol. Inorg. Chem.

[7] K. Möbius, A. Savitsky, C. Wegener, M. Plato, M. Fuchs, A. Schnegg, A. A. Dubinskii, Y. A. Grishin, I. A. Grigor'ev, M. Kühn, D. Duché, H. Zimmermann, and H.-J. Steinhoff, Magn. Res, Chem. **43**, S4 (2005).

[8] Y. He, J.-Y. Chen, J. R. Knab, W. Zheng, and A. G. Markelz, Biophys. J. **100**, 1058 (2011).

[9] E. L. Hahn, Phys. Rev. **80**, 580 (1950).

[10] G. V. Kozlov, S. P. Lebedev, A. A. Mukhin, A. S. Prokhorov, I. V. Fedorov, A. M. Balbashov, and I. Y. Parsegov, IEEE Trans. Magn. **29**, 3443 (1993).

[11] K. Yamaguchi, M. Nakajima, and T. Suemoto, Phys. Rev. Lett. **105**, 237201 (2010).

[12] T. Kampfrath, A. Sell, G. Klatt, A. Pashkin, S. Mährlein, T. Dekorsy, M. Wolf, M. Fiebig, A. Leitenstorfer, and R. Huber, Nat. Photonics **5**, 31 (2011).

[13] T. Li, A. Patz, L. Mouchliadis, J. Yan, T. A. Lograsso, I. E. Perakis, and J. Wang, Nature (London) **496**, 69 (2013).

[14] M. Rini, N. Dean, J. Itatani, Y. Tomioka, Y. Tokura, R. W. Schoenlein, and A. Cavalleri, Nature (London) **449**, 72 (2007).

[15] W. Eerenstein, N. D. Mathur, and J. F. Scott, Nature (London) **442**, 759 (2006).

[16] J. Simon, H. Tanji, S. Ghosh, and V. Vuletić, Nat. Phys. **3**, 765 (2007).

[17] C. D. Stanciu, F. Hansteen, A. V. Kimel, A. Kirilyuk, A. Tsukamoto, A. Itoh, and T. Rasing, Phys. Rev. Lett. **99**, 047601 (2007).

[18] A. V. Chumak, V. I. Vasyuchka, A. A. Serga, and B. Hllebrands, Nat. Phys. **11**, 453 (2015).

[19] A. V. Kimel, B. A. Ivanov, R. V. Pisarev, P. A. Usachev, A. Kirilyuk, and T. Rasing, Nat. Phys. **5**, 727 (2009).

[20] A. Kirilyuk, A. V. Kimel, and T. Rasing, Rev. Mod. Phys. **82**, 2731 (2010).

[21] S. Wienholdt, D. Hinzke, and U. Nowak, Phys. Rev. Lett. **108**, 247207 (2012).

[22] T. Kampfrath, K. Tanaka, and K. A. Nelson, Nat. Photonics **7**, 680 (2013).

[23] Y. Mukai, H. Hirori, T. Yamamoto, H. Kageyama, and K. Tanaka, New J. Phys. **18**, 013045 (2016).

[24] H. Lütgemeier, H. G. Bohn, and M. Brajczewska, J. Magn. Magn. Mater. **21**, 289 (1980).

[25] R. M. White, R. J. Nemanich, and C. Herring, Phys. Rev. B **25**, 1822 (1982).

[26] S. E. Hahn, A. A. Podlesnyak, G. Ehlers, G. E. Granroth, R. S. Fishman, A. I. Kolesnikov, E. Pomjakushina, and K. Conder, Phys. Rev. B **89**, 014420 (2014).

[27] See Supplemental Material for supporting measurements and details of the data analysis including: lattice structure and spin order, experimental setup, field dependence of nonlinear spectral signals, numerical simulations, simulated F mode 2D spectrum,double-sided Feynman diagrams and frequency-vector representations, origins of second-order signals, which includes Ref. [41-44].

[28] A. Nahata, D. H. Auston, T. F. Heinz, and C. Wu, Appl. Phys. Lett. **68**, 150 (1996).

[29] K.-L. Yeh, M. C. Hoffmann, J. Hebling, and K. A. Nelson, Appl. Phys. Lett **90**, 171121 (2007).

[30] H. Hirori, A. Doi, F. Blanchard, and K. Tanaka, Appl. Phys. Lett. **98**, 091106 (2011).

[31] M. Woerner, W. Kuehn, P. Bowlan, K. Reimann, and T. Elsaesser, New J. Phys. **15**, 025039 (2013).

[32] A. Morello, P. C. E. Stamp, and I. S. Tupitsyn, Phys.

Rev. Lett. **97**, 207206 (2006).

[33] P. A. Fleury and R. Loudon, Phys. Rev. **166**, 514 (1968).

[34] G. F. Herrmann, J. Phys. Chem. Solids **24**, 597 (1963).

[35] P. C. Planken, H.-K. Nienhuys, H. J. Bakker, and T. Wenckebach, J. Opt. Soc. Am. B **18**, 313 (2001).

[36] S. I. Kiselev, J. C. Sankey, I. N. Krivorotov, N. C. Emley, R. J. Schoelkopf, R. A. Buhrman, and D. C. Ralph, Nature (London) **425**, 380 (2003).

[37] S. Baierl, J. H. Mentink, M. Hohenleutner, L. Braun, T.-M. Do, C. Lange, A. Sell, M. Fiebig, G. Woltersdorf, T. Kampfrath, and R. Huber, Phys. Rev. Lett. **117**, 197201 (2016).

[38] M. Shalaby and C. P. Hauri, Nat. Commun. **6** (2015).

[39] P. Hamm and M. Zanni, *Concepts and methods of 2D infrared spectroscopy* (Cambridge University Press, Cambridge, UK, 2011).

[40] S. H. Baek, H. W. Jang, C. M. Folkman, Y. L. Li, B. Winchester, J. X. Zhang, Q. He, Y. H. Chu, C. T. Nelson, M. S. Rzchowski, X. Q. Pan, R. Ramesh, L. Q. Chen, and C. B. Eom, Nat. Mater. **9**, 309 (2010).

[41] S. Casalbuoni, H. Schlarb, B. Schmidt, P. Schmüser, B. Steffen, and A. Winter, Phys. Rev. Spec. Top. Accel. Beams **11**, 072802 (2008).

[42] G. F. Herrmann, Phys. Rev. **133**, A1334 (1964).

[43] J. Stöhr and H. C. Siegmann, *Magnetism: from Fundamentals to Nanoscale Dynamics* (Springer, New York, USA, 2006).

[44] K. Kocharyan, R. Martirosyan, V. Prpryan, and E. Sarkisyan, Sov. Phys. JETP **59**, 373 (1984).